Effects of Moist Convection on Hurricane Predictability

FUQING ZHANG

Department of Meteorology, The Pennsylvania State University, University Park, Pennsylvania

JASON A. SIPPEL*

Department of Atmospheric Science, Texas A&M University, College Station, Texas

ABSTRACT

This study exemplifies inherent uncertainties in deterministic prediction of hurricane formation and intensity. Such uncertainties could ultimately limit the predictability of hurricanes at all time scales. In particular, this study highlights the predictability limit due to the effects on moist convection of initial-condition errors with amplitudes far smaller than those of any observation or analysis system. Not only can small and arguably unobservable differences in the initial conditions result in different routes to tropical cyclogenesis, but they can also determine whether or not a tropical disturbance will significantly develop. The details of how the initial vortex is built can depend on chaotic interactions of mesoscale features, such as cold pools from moist convection, whose timing and placement may significantly vary with minute initial differences. Inherent uncertainties in hurricane forecasts illustrate the need for developing advanced ensemble prediction systems to provide event-dependent probabilistic forecasts and risk assessment.

1. Introduction

Hurricanes are one of deadliest and costliest natural hazards, with total losses topping $100 billion for the first time in 2005 (Pielke et al. 2008). Accurate predictions of hurricanes therefore have enormous economic value, and demand is increasing for more accurate forecasts with longer lead times and more precise warnings to minimize losses due to hurricane preparation and evacuation as well as to destruction. Over the past decade, significant progress has been made in short-range (up to 5 days) track forecasts of tropical cyclones. The current-day average 48-h forecast position is as accurate as a 24-h track forecast 10 yr ago (Franklin 2004).

Unfortunately, today's intensity predictions continue to have significant error. There is virtually no improvement in our ability to predict hurricane intensity in terms of minimum sea level pressure, maximum wind speed, or amount of precipitation (Houze et al. 2007), and we therefore have very limited skill in predicting tropical cyclone formation, rapid intensification, fluctuation, or decay (Elsberry et al. 2007). The discrepancy between track and intensity forecast accuracy of tropical cyclones may be due to the fact that track is largely dependent on the large-scale environment, which has become more and more predictable with rapid advances in numerical weather prediction models and better observing systems. Meanwhile, intensity is largely determined by far less predictable internal dynamics that are only modulated by the larger-scale environment (Holland 1997; Willoughby 1999; Emanuel 1999). Upscale growth of moist convection, such as in the form of vortical hot towers (VHTs), may play a critical role in internal dynamics (Hendricks et al. 2004; Krishnamurti et al. 2005; Montgomery et al. 2006). Therefore, limited predictability of moist convection may also ultimately limit the predictability of tropical cyclones, as is the case for extratropical cyclones (Zhang et al. 2002, 2003, 2007) or continental warm-season mesoscale convective systems (Zhang et al. 2006; Hawblitzel et al. 2007; Bei and Zhang 2007).

The current study follows the preceding work of Sippel and Zhang (2008, hereafter SZ08) and examines

* Current affiliation: NASA Goddard Space Flight Center, Greenbelt, Maryland.

Corresponding author address: Dr. Fuqing Zhang, Dept. of Meteorology, The Pennsylvania State University, University Park, PA 16802.
E-mail: fzhang@psu.edu

the predictability of a low pressure system over the Gulf of Mexico just west of Florida that preceded Hurricane Alex (2004). This Gulf low never developed into a tropical cyclone, although the National Hurricane Center highlighted its potential for development in their tropical weather outlooks. SZ08 studied the disturbance with short-range ensemble forecasts from a mesoscale model at low resolution with parameterized moist convection and at high resolution with explicit convection. Taking advantage of discrepancies between ensemble members, they used statistical correlation to elucidate why some ensemble members strengthened the disturbance into a tropical cyclone and others did not. They found that the combination of deep moisture and high CAPE yielded more active initial convection and quick intensification during the first 6–12 h of some ensemble members. Thus, differences in deep moisture and CAPE caused much of the initial ensemble spread. Discrepancies present at 12 h were further amplified by differences in convection related to latent heat fluxes and the wind-induced surface heat exchange (WISHE) process (Rotunno and Emanuel 1987). The current study further examines the effect of moist convection in leading to the differences between two extreme members of the above ensemble: member 6, which developed a strong tropical storm, and member 20, which remained very weak after 36 h.

This study analyzes the effects of initial-condition differences on both larger-scale structure and smaller-scale variations during tropical cyclone formation. Although the results of SZ08 showed that that large-scale thermodynamics play an important role in tropical cyclone formation, their mesoscale area averages preclude insight into the importance of smaller-scale features such as VHTs, which can also be important for genesis (Hendricks et al. 2004; Montgomery et al. 2006; Tory et al. 2006a,b). This paper investigates how *both* larger mesoscale variations and VHT generation/evolution are impacted by initial-condition error. For a more thorough review of observations and the theory of tropical cyclone formation, see the introduction of SZ08.

2. Overview of the ensemble simulations

Two 20-member ensemble simulations are examined in this study. The coarse-resolution ensemble (30KM; the same as in SZ08) has a 30-km horizontal grid spacing (a typical resolution of the current-generation global weather prediction models) with parameterized convection, whereas the high-resolution ensemble (3.3KM; the same as CTRL in SZ08) employs three two-way nested model domains and has an effective grid spacing of 3.3 km over the tropical cyclone genesis region. Thus,

the 3.3KM ensemble permits explicit simulation of moist convection (hereafter loosely referred to as "cloud-resolving"). Both experiments use the fifth-generation Pennsylvania State University–National Center for Atmospheric Research (NCAR) Mesoscale Model (MM5; Dudhia 1993) starting at 0000 UTC 30 July 2004; 3.3KM and 30KM are integrated for 36 and 72 h, respectively. As in SZ08, the Mellor–Yamada planetary boundary layer (PBL) scheme and Reisner microphysics scheme are used on all domains. Also, the Grell cumulus scheme is used to represent cumulus convection in 30KM, but it is not used on the 10- and 3.3-km domains in 3.3KM.

The initial ensemble perturbations are the same for both ensembles and were generated through perturbing the reference National Centers for Environmental Prediction (NCEP) final (FNL) analysis with random but balanced noise derived from the NCEP background error statistics implanted in the MM5 three-dimensional variational data assimilation system (Barker 2005). Figure 1 shows the vertical distribution of the initial ensemble spread, which is 0.7–1.2 m s^{-1} for zonal wind u, 0.3–0.5 K for temperature T and 2%–4% for relative humidity (RH). These values are smaller in amplitude than the root-mean-square (rms) differences between the NCEP–NCAR reanalysis (NNRP) and the European Centre for Medium-Range Weather Forecasts (ECMWF) Re-Analysis (ERA) (dotted) and differences between the NCEP–NCAR reanalysis and the NCEP FNL analysis (dotted–dashed) over the MM5 domain at this time. Because such differences can be used as rough, conservative estimates of typical analysis errors at leading operational centers, the spread here is generally less than the analysis error. Furthermore, Fig. 2 shows that the initial surface and 700-hPa wind, temperature, and mixing-ratio differences between extreme members 6 and 20 (detailed below) are smaller in magnitude and comparable in scale to differences between the NNRP and ERA reanalyses over the southeastern two thirds of the display domain. This area covers the initial Gulf low and the precursor of Alex (2004). Thus, the initial discrepancies between these two extreme members are comparable to realistic analysis uncertainties in the large-scale environment over the ocean. Additional analysis uncertainties related to the mesoscale and microscale structure of the tropical disturbances, along with errors in the forecast model, may lead to even stronger forecast divergence and thus further limit hurricane predictability. However, the current study focuses only on the effect of large-scale environment initial uncertainty on the predictability of tropical cyclones.

Over the first 36-h integration of 30KM, many ensemble members develop the Gulf low pressure system into a tropical cyclone (and even hurricane) with a
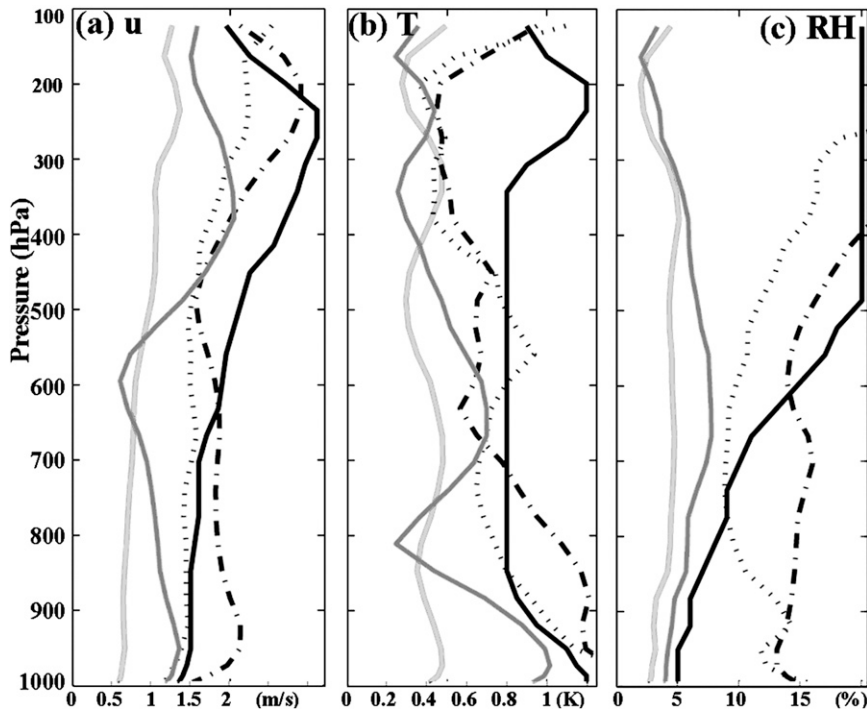
FIG. 1. Vertical distribution of the initial ensemble spread (light gray) for (a) zonal wind u (m s^{-1}), (b) temperature (K) and (c) relative humidity (%) over domain 1. Also plotted are the vertical distributions of the default observational errors (black) as well as the rms differences between members 6 and 20 (dark gray), between the NCEP–NCAR reanalysis and the ECMWF analysis (dotted), and between the NCEP–NCAR reanalysis and the NCEP FNL analysis (dotted–dashed).

variety of forecast tracks. SZ08 showed that error grew quite rapidly with this system, and Fig. 3 shows extreme uncertainties in the intensity forecast of the Gulf low measured in terms of the ensemble spread of minimum sea level pressure (SLP) and maximum surface wind speeds valid at 36 and 72 h. The minimum SLP at 36 h among members of 30KM varies from 1010 hPa in member 20 to 996 hPa in member 6, and the maximum surface wind varies from 13 to 26 m s^{-1}. Even stronger variations occur at 72 h for the minimum SLP (from 1007 to 987 hPa) and maximum surface winds (from 17 to 33 m s^{-1}). Although member 20 remains the weakest storm, a few other members become significantly stronger than member 6 at 72 h (Fig. 3). These intensity differences appear in spite of the fact that large-scale initial-condition uncertainty is realistic for the initial analyses (because it was drawn from the default background error statistics) and rather small compared to typical sounding observational and analysis errors (Fig. 1).

The drastic forecast differences for the Gulf low in 30KM are also evident in 3.3KM, and members 6 and 20 continue to be extremes in terms of minimum SLP (1008

and 994 hPa, respectively). Although these two members are not absolute extremes at 36 h in terms of maximum wind speed (Fig. 3), they remain at nearly opposite ends of the ensemble. The maximum surface wind in the strongest member (8) in Fig. 3 is 33 m s^{-1}, which is above the threshold for a category-1 hurricane and 7 m s^{-1} stronger than member 6. However, the overall difference between members 6 and 8 may not be particularly significant in light of the strong spatial and temporal wind variability in the vicinity of convective bursts in 3.3KM (not shown). Minimum SLP does not exhibit this degree of sensitivity, and indeed it is nearly identical in members 6 and 8 (Fig. 3). Likewise, the slight difference in wind between member 20 and the weakest ensemble member is also insignificant.

Although the results in Fig. 3 appear to contradict the finding in SZ08 that 30KM has slightly stronger storms with more spread at 36 h, it must be kept in mind that Fig. 3 displays intensity metrics for 3.3KM on its 3.3-km grid. Meanwhile, the calculations in SZ08 were performed on the 30-km grid for consistency purposes. The spread of 3.3KM is indeed smaller than that of 30KM on the scale of the 30-km grid, but there are more substantial
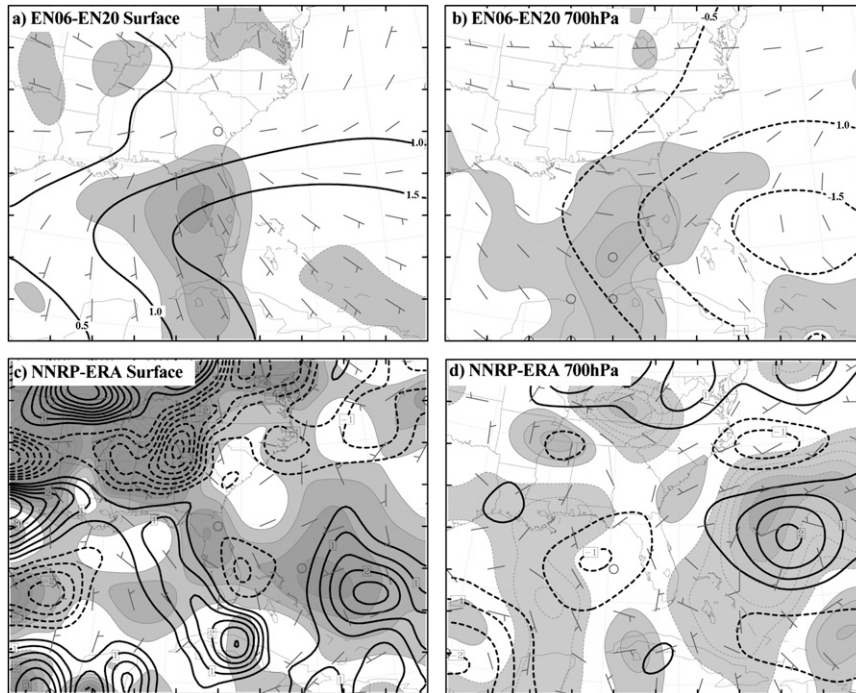
FIG. 2. Difference between surface and 850-hPa temperature (thick; every 0.5K), mixing ratio (thin lined and shaded; every 0.5 g kg^{-1}) and horizontal wind vectors (full barb 5 m s^{-1}) between (a),(b) ensemble members 6 and 20 at the initial time and (c),(d) the NCEP–NCAR and ECMWF global reanalyses interpolated to the MM5 grids.

differences between ensemble members in 3.3KM in the vicinity of convection at smaller scales.

3. Sensitivity experiments

In this section we begin to explore the dynamics that lead to drastic differences in storm development between members 6 and 20 through initial-condition sensitivity experiments. For simplicity, we first define the nondeveloped member 20 to have an initial perturbation of zero (hereafter, member 20 is also called QRT0). We also define the difference between members 6 and 20 for all prognostic variables as one unit state vector (the "difference vector"). Thus, the perturbation magnitude for member 6 is one unit, or four quarters (thus, member 6 is also called QRT4). Also performed are a series of sensitivity experiments, each with an initial perturbation added to QRT0 that varies in amplitude from −0.5 to 1.5 in units of the difference vector. For example, an initial perturbation value of 1.5 corresponds to adding 1.5 times (i.e., six quarters) the initial difference between QRT0 and QRT4 to the reference experiment QRT0 (these are the conditions of experiment QRT6), and a perturbation value of −0.5 corresponds to subtracting the half the difference from QRT0

(i.e., experiment QRTm2). Values of 0.5 and 0.75 correspond to experiments QRT2 and QRT3, which respectively add perturbations to QRT0 with amplitudes of two and three quarters that of the difference vector. Experiments QRTm1 and QRT5 respectively correspond to perturbations of −0.25 and 1.25.

Figures 4 and 5 demonstrate that the above simulations can be clearly grouped as "developing" and "nondeveloping." Figure 4 shows sensitivity of the 36-h minimum SLP change to adding different initial perturbations in both parameterized-convection (30-km) and cloud-resolving (3.3-km) experiments. The 36-h minimum SLP has a near-bimodal distribution with strong tropical storms (similar to QRT4) for initial perturbations greater than 0.5 and weak tropical disturbances (as is the case in QRT0) for initial perturbations less than 0.5. The transition zone in Fig. 4 is very narrow, and a change as small as one quarter of the difference vector (e.g., from QRT2 to QRT3) distinguishes whether or not a well-organized tropical cyclone will form. Figure 5, which shows the 36-h surface wind and SLP from QRT0, QRT2, QRT3, and QRT4, further demonstrates the narrow transition zone. QRT3 and QRT4 are both near category-1 hurricane strength, and each has an impressive primary rainband and a
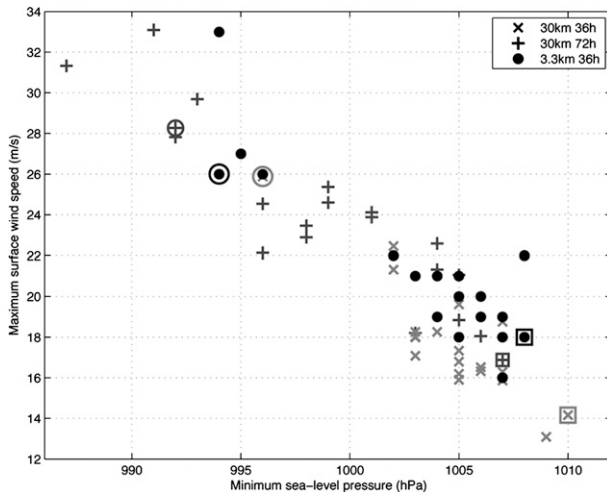
FIG. 3. Minimum sea level pressure vs maximum surface winds for the Gulf low simulated by the ensembles initialized at 0000 UTC 30 Jul 2004. The individual markers correspond to forecasts by each member of 30KM valid at 36 h (×) and 72 h (+) and for ensemble 3.3KM at 36 h (●). Member 6 (20)—that is, simulation QRT4 (QRT0)—is highlighted with an additional circle (square).

FIG. 4. Sensitivity of the 36-h minimum sea-level pressure to the initial-perturbation amplitude for the 30-km (gray) and 3.3-km (black) simulations, respectively. The x axis depicts the initial perturbation magnitude scaled by the difference vector, which is the initial difference for all prognostic variables between QRT4 (circle) and QRT0 (square).

nearly closed eyewall (not shown directly, but they can be implied from the wind field). Meanwhile, there is virtually no tropical development in QRT0, whereas QRT2 forms a generally unorganized tropical cyclone.

The simulations with developing systems can also be distinguished in terms of organization as early as 6 h, a result that will be discussed in much more detail in sections 4 and 5. For now, it is sufficient to say that simulations QRT2 through QRT6 develop both larger-scale circulations and strong 15–30-km-wide vortices, with the latter being referred to as VHTs when they are associated with active updrafts. Examples of VHTs in QRT5 and QRT6 at 9 h are shown in Figs. 6a,b, where 985-hPa θ_e, wind vectors, and vertical vorticity are shown along with 500-hPa vertical velocity. The towers of strong vorticity are generally associated with updrafts (as in anomalies A1, B1, C1, B2, and C2), although sometimes the vorticity remains long after the updraft dies (as in A2; such features will be referred to as remnant vortices because VHTs must be associated with updrafts). Some VHTs congregate in groups to build slightly larger-scale vortices (e.g., C1 and C2), and when such clusters of vortices occur at the approximate circulation center, they are loosely referred to as the cyclone core (e.g., see the circulation centers in Figs. 6c,d). These clusters of VHTs might be akin to the convective burst vortices discussed in Sippel et al. (2006). Both QRT0 and QRT1 also initially develop weaker larger-scale circulations and a few small-scale vorticity anomalies near their limited convective cells. However, their

small-scale features are weak, isolated, and ephemeral. Meanwhile, QRTm1 and QRTm2 take 12–18 h to develop even a very weak larger-scale circulation.

Finally, in light of the small initial-condition differences between QRT0 and QRT4, the stark differences between QRT0 and QRT4 in terms of cyclone development are somewhat alarming. In particular, the initial rms difference between QRT0 and QRT4 is considerably smaller than NCEP-assumed observational errors and differences between global analyses of leading operational centers for all variables at nearly every vertical level (Figs. 1 and 2). The large difference in outcome due to small initial uncertainty in the large-scale environment further highlights the extreme difficulty associated with deterministic prediction of hurricane formation and intensity.

4. Effects of moist convection: Storm scale

In the previous section, it was demonstrated that a sharp transition occurs both in the 30-km and 3.3-km simulations, and in the following section we will examine in detail the role of moist convection in the extreme sensitivity of model solutions to very small initial-condition differences between the 3.3-km, cloud-resolving simulations shown in Fig. 4 (although the main focus will be on those from Fig. 5). Our choice of initial variables and parameters to examine is motivated by the findings of SZ08. In particular, Fig. 7 shows the time evolution of responses to the different initial conditions in all simulations in Fig. 4 averaged over a
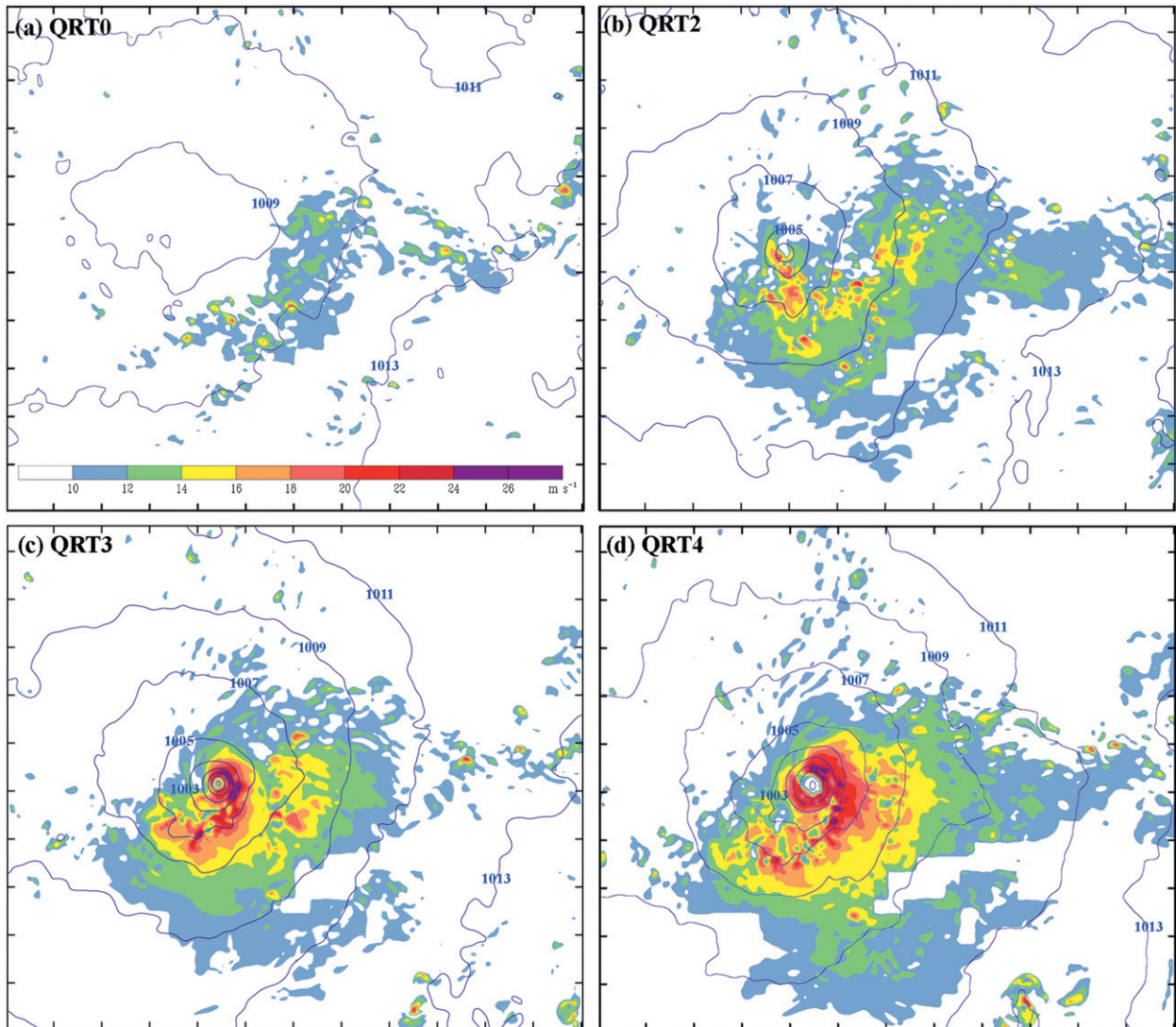
FIG. 5. Comparison of the 36-h surface wind speed (only >10 m s^{-1}, color filled every 2 m s^{-1}) and sea level pressure forecasts of the Gulf low in the 3.3-km simulations (a) QRT0, (b) QRT2, (c) QRT3, and (d) QRT4. The sea level pressure (contoured every 2 hPa) is smoothed nine times with a five-point smoother. Tick marks denote a horizontal distance of 100 km.

300 km × 300 km box area (hereafter referred to as a "storm-scale" average)[1] except for maximum surface

vorticity (Fig. 7f) and wind speed (Fig. 7d). SZ08 found that the initial most unstable CAPE (MUCAPE)[2] was well correlated to cyclone intensification, but this study instead examines surface θ_e. Initial MUCAPE and θ_e were strongly correlated at early times in SZ08, so differences in θ_e represent similar differences in MUCAPE. In addition, surface θ_e has the added benefit of demonstrating cold pool strength and the extent of PBL

---

[1] Before convection begins, the box center is near the 700-hPa circulation center (i.e., where convective initiation occurs) in QRT0 through QRT6. Thereafter, the box center follows the surface to 850-hPa approximate vorticity center in those same simulations. For illustrative purposes, some attempt is made to follow the low-level vorticity core that develops during the first 6 h until it is indiscernible. Because convection is almost completely inactive in QRTm1 and QRTm2, a surface low is very slow to form. Therefore, the box center in those simulations follows that of QRT0 for the entire simulation. Only small changes in storm-scale averages occur if the box center is defined by other metrics. The center in all figures that use the 300 km × 300 km Lagrangian domain follows the same box center used to compute averages in Fig. 7.

[2] MUCAPE is computed as the CAPE for the parcel in each column with maximum equivalent potential temperature within the lowest 3000 m. Following the recommendation of Doswell and Rasmussen (1994), virtual potential temperature is used in this calculation.
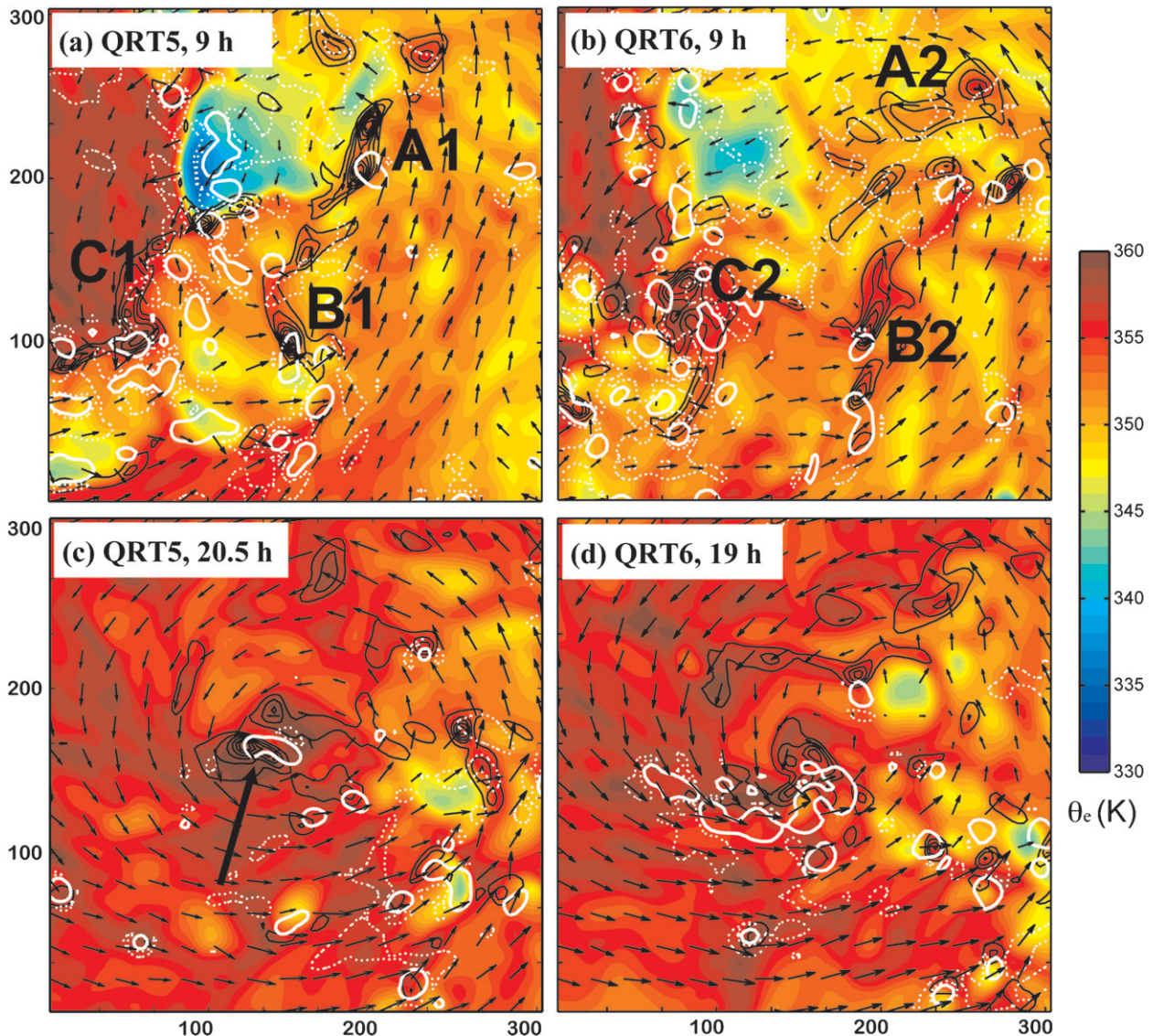
FIG. 6. The 985-hPa wind vectors (scaled differently in each panel), absolute vorticity (black contours every 5×10^{-4} s^{-1} beginning at 5×10^{-4} s^{-1}), θ_e (color filled every 1 K), and 500-hPa vertical velocity (-0.25 m s^{-1} contoured in dotted white; 1.0 m s^{-1} contoured in solid white). Variables are plotted (a),(b) at 9 h over the storm-scale region in simulations (a) QRT5 and (b) QRT6; (c) at 20.5 h in QRT5; and (d) at 19 h in QRT6. Axes are labeled every 100 km. VHTs, VHT clusters, and remnant vortices are labeled in bold in (a) and (b), and the arrow in (c) points to the remnant vortex from B1.

recovery after cold pool formation. Meanwhile, storm-scale 700-hPa vertical velocity w and 3-h precipitation totals demonstrate differences in convection, and average wind speed and vorticity show differences in overall strength on the system scale. Maximum surface wind speed and vorticity are metrics of system strength on local scales, which along with minimum sea level pressure are also common indices of tropical cyclone intensity.

In a manner consistent with SZ08, storm intensity appears to vary with initial θ_e differences and the amount of initial precipitation that falls. Simulations with higher initial instability (Fig. 7h) have stronger mean upward velocity at 700 hPa through 6 h (Fig. 7a), and they generate more precipitation during the first 9 h (Fig. 7b). Likewise, these same simulations have generally stronger storm-scale surface wind speeds and vorticity by 6–12 h (Figs. 7c–f). The apparent inability to develop a cyclone without an initial round of convection is quite evident by the similarly low storm-scale winds and vorticity in QRT0, QRTm1, and QRTm2.
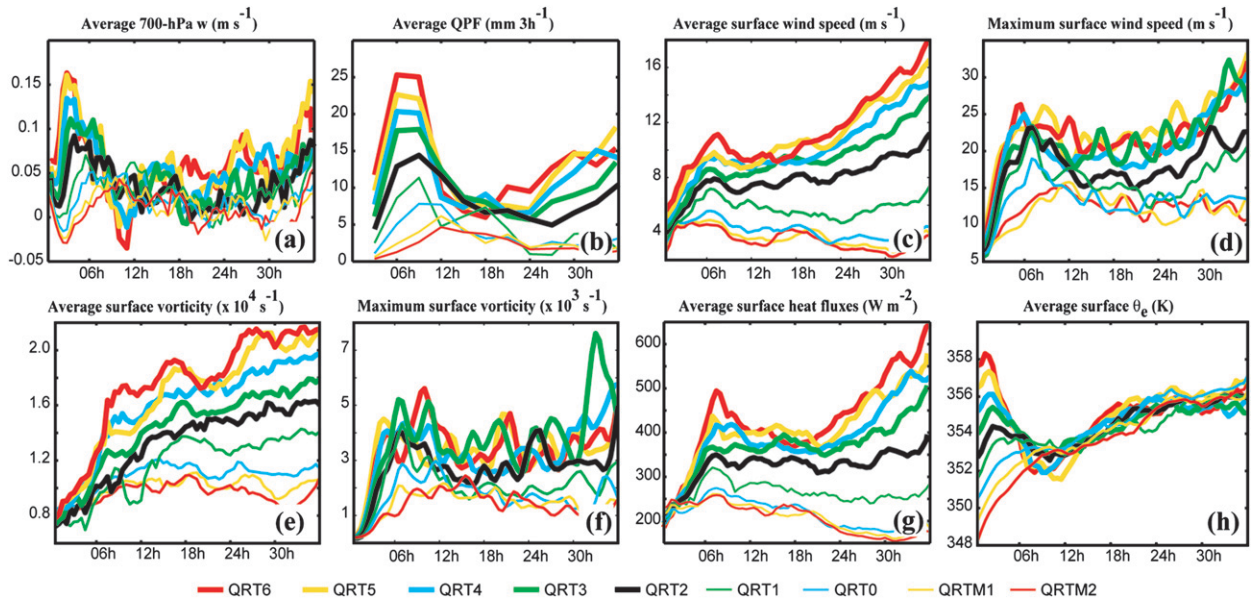
FIG. 7. Time evolution of storm-scale averaged (a) 700-hPa vertical velocity (m s^{-1}), (b), 3-h accumulated precipitation (mm), (c) surface wind speed (m s^{-1}), (e) surface vorticity ($\times 10^{-4}$ s^{-1}), (g) total (sensitive + latent) surface heat fluxes (W m^{-2}), and (h) surface θ_e (K), as well as (d) maximum surface wind (m s^{-1}; smoothed twice with a 3-point smoother) and (f) maximum surface vorticity ($\times 10^{-3}$ s^{-1}; smoothed twice with a three-point smoother) in all 3.3-km simulations shown in Fig. 4.

a. Convective instability and convection

While the initial differences in most variables in Fig. 7 are quite small compared to their later differences, differences in surface θ_e (due to both temperature and moisture differences) are considerably larger at the initial time than they are at later times. For example, initial surface θ_e in QRT4 (i.e., member 6) is a little more than 4.5 K higher than in QRT0 (member 20), but it decreases to less than 2 K at later times. The initial difference in surface θ_e between QRT0 and QRT4 (Fig. 8a), although seemingly large, is comparable to the difference between NCEP and ECMWF global reanalyses over this region (Fig. 8b). This difference therefore grossly represents the realistic large-scale initial-condition uncertainties in tropical cyclone prediction. The following discussion will show that the underlying cause for diminishing θ_e variation is that convection tends to equilibrate convective instability among the simulations. Meanwhile, the same differences in convection tend to increase variation with other variables and metrics of strength.

If, as found in SZ08, higher initial surface-based instability results in more precipitation, then it must do so as a result of more intense and/or widespread updrafts. Although mean 700-hPa w is indeed stronger in simulations with higher initial instability, general updraft (and downdraft) characteristics are not clear from such a mean. To better understand early updrafts, the anal-

ysis in Figs. 9a,b is undertaken by first calculating vertical mass flux per unit area at every point and every σ level in the storm-scale region every 30 min during 0–6 h, 6–9 h, and 0–9 h. The first time period encompasses the strongest convection in all simulations and ends generally before strong cold pools form, the second period begins about when significant cold pools begin to form, and the sum of the two periods spans the duration of the heaviest precipitation for all simulations in Fig. 7. Mass flux per unit area is calculated by multiplying vertical velocity by density at each grid point. Gridpoint values are sorted into 0.25 m s^{-1} vertical velocity bins (from −2.5 to 14 m s^{-1}), with each σ level retaining its own set of bins. Vertical mass flux is then summed for all grid point w values in each bin, and the difference in resulting sums between QRT4 and QRT3 and between QRT3 and QRT2 is contoured as a function of updraft velocity and height. Positive values in Figs. 9a–c indicate greater upward flux in QRT4 than QRT3, and positive values in Figs. 9d–f indicate greater upward flux in QRT3 than QRT2.

Convection is clearly stronger during the first 6 h in simulations with higher instability. Figures 9a and 9d show that net 0–6-h upward mass flux increases incrementally from QRT2 to QRT4 for nearly all updraft speeds at any given level. An exception is that some of the stronger updrafts in QRT3 are stronger than those in QRT4, but this represents only a small minority of updrafts. The greater upward fluxes in QRT4 indicate
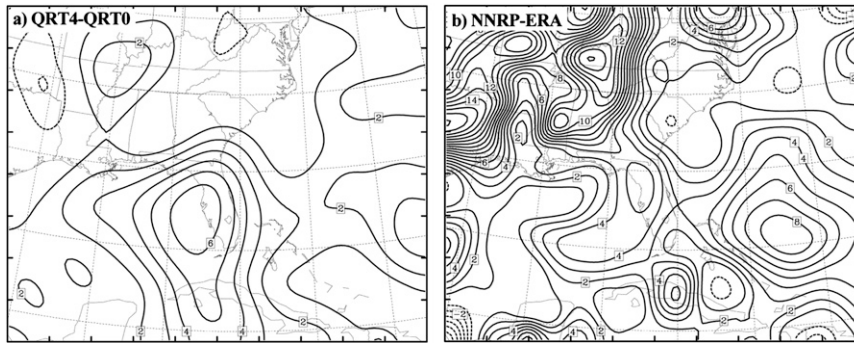
FIG. 8. The initial difference in surface θ_e (every 1 K; negative, dotted) between (a) QRT0 and QRT4 and (b) between NCEP/NCAR reanalysis (NNRP) and ECMWF reanalysis (ERA) interpolated to the MM5 grids.

that updrafts of a particular intensity cover a larger area and/or last longer in that simulation. Likewise, QRT2 has weaker upward mass flux than the other two simulations.

b. Cold pools

Also associated with the stronger convection in the more unstable simulations are stronger downdrafts that lead to substantial drops in surface θ_e. Although θ_e rises during the first few hours because of horizontal advec-tion and oceanic heat fluxes, it drops proportionally with 6-h precipitation totals after convective initiation. For example, although simulations QRT4 through QRT6 have higher initial θ_e, they also have more initial precipitation, and downdrafts quickly cool their sur-face to a value below that seen in the other simulations (Fig. 7h). As a testament to the strong downdrafts in QRT4, Fig. 9d shows that downward mass flux is un-ambiguously stronger for all downdraft speeds at all levels in QRT4 than in QRT3. Likewise, QRT3 has
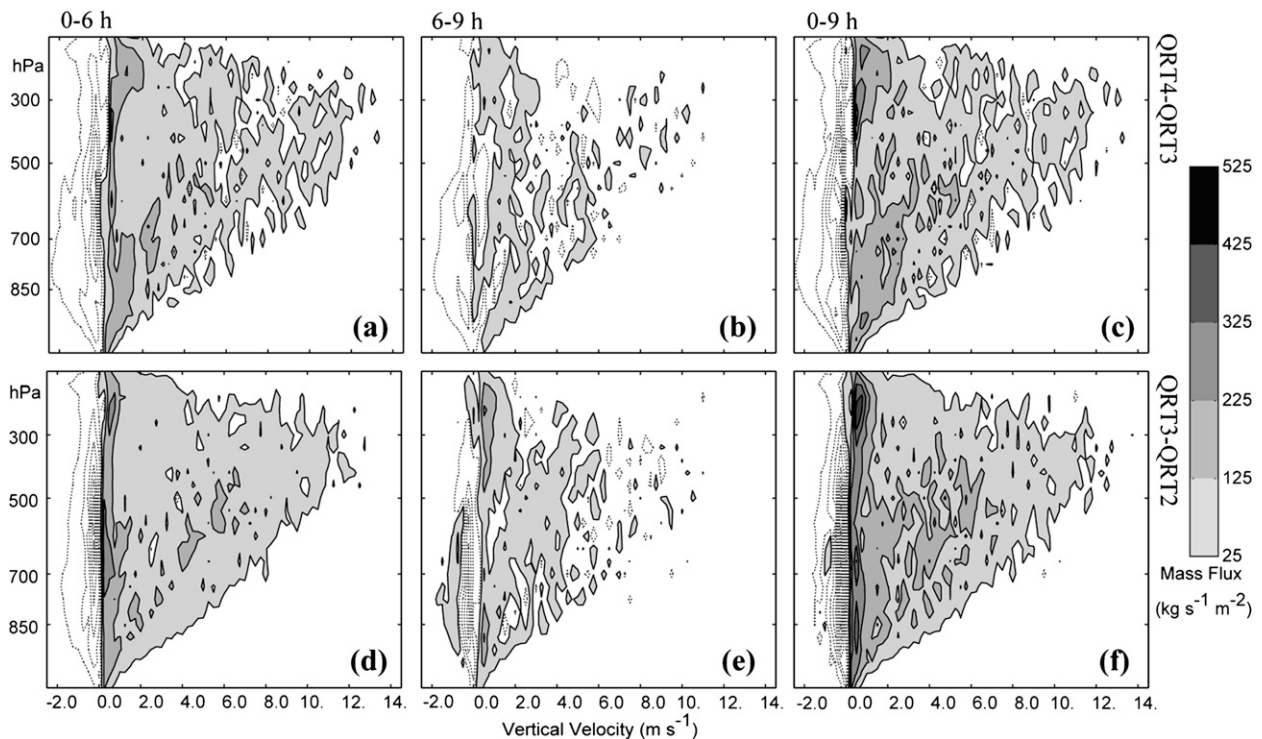
FIG. 9. Difference in total vertical mass flux per unit area between (a)–(c) QRT4 and QRT3 and (d)–(f) QRT3 and QRT2 as a function of vertical velocity (m s^{-1}; x axis) and height. Differences are shown from (a),(d) 0–6 h, (b),(e) 6–9 h and (c),(f) 0–9 h with positive (negative) differences shaded (dashed/contoured) every 100 kg s^{-1} m^{-2} beginning at 25 (-25) kg s^{-1} m^{-2}.
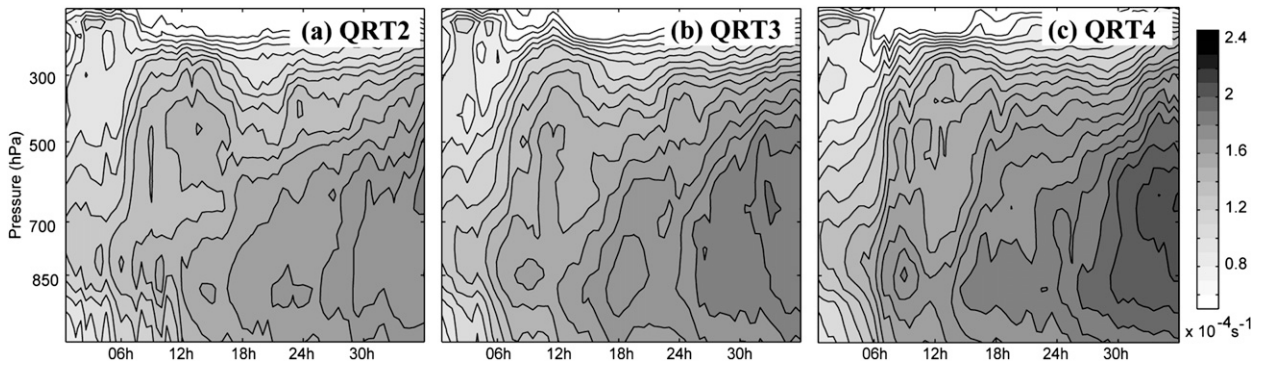
FIG. 10. Evolution of the vertical distribution of vertical vorticity (every $2 \times 10^{-5}\,\mathrm{s}^{-1}$) averaged over the storm-scale region for (a) QRT2, (b) QRT3, and (c) QRT4.

generally stronger downward mass flux than QRT2, especially during the first 6 h.

An interesting result in Fig. 7h is that the cold pool strength in QRT3 is more similar to QRT2 than the other convectively active cases from 6–12 h. Although the reason for this is not entirely clear, it will be discussed in more detail in section 5. For now, the important result is that QRT3 is somewhat of an outlier because it has substantially more convection than QRT2, but its cold pool strength is comparable to that of QRT2.

Widespread colder surface air eventually diminishes updrafts near the centers, especially in QRT4 through QRT6. Figure 9b reveals that the 6–9-h total updraft flux in QRT3 is approximately equal to that in QRT4 over much of the troposphere, which is a substantial change from the 0–6-h total in Fig. 9a. The difference between Figs. 9a and 9b is a result of the surface cold pool in QRT4 reducing instability and therefore the number of strong updrafts near the center after 6 h. Although mean vertical motion in QRT4 remains positive through 9 h (Fig. 7a), it becomes negative for a period between 9 and 12 h. There is also subsidence from 9–12 h in QRT5 and QRT6, and storm-scale 700-hPa w is lower in QRT4 through QRT6 than in any of the other simulations during this period (Fig. 7a). Concomitantly, QRT4 through QRT6 generally produce less precipitation than QRT2 and QRT3 from 9 to 15 h (Fig. 7b). In addition, simulations QRT2 and QRT3 exhibit substantial drops in θ_e and precipitation totals due to cold downdrafts by 12 h, and the period from 12 to 24 h is convectively the least active period for all developing simulations.

c. Vorticity production: A response to convection

Simulations with greater net vertical mass flux should also have stronger production of vertical vorticity via stretching deformation. Vorticity budgets (not shown) and the time evolution of storm-scale vertical vorticity (displayed as a function of height in Fig. 10) indicate that there indeed is an approximately linear tendency for vorticity to strengthen from simulation QRT2 to QRT4. A vorticity maximum initially between 700 and 850 hPa grows stronger and deeper with time, and around 6 h there is a rapid increase in storm-scale vorticity through the entire depth of the troposphere in all three simulations. Thus, incrementally higher precipitation totals in QRT3 and QRT4 lead to incrementally higher vorticity values through much of the troposphere (consistent with SZ08).

The response in storm-scale vorticity to the widespread downdrafts and cold pools can also be seen in Fig. 10. Storm-scale vorticity decreases somewhat after 9 h in QRT3 (Fig. 10b), and it decreases strongly in QRT4 (Fig. 10c). This is consistent with stronger downdrafts and negative mean 700-hPa w in QRT4.

d. Recovery period and beyond

In the absence of widespread convection, the PBL recovers from the prolific cold pools present at 12 h. When θ_e reaches 355–356 K (at about 24 h), persistent convection begins again at the circulation centers of the active simulations. As rainfall begins to increase again in QRT2 through QRT4, the vortices grow stronger and deeper (Fig. 10), with higher surface wind speeds and heat fluxes (Fig. 7). Simulations QRT3 through QRT6 all exhibit impressive increases in maximum wind speed after 24 h, and peak surface winds at 36 h are about 50% higher than those at 24 h.

Interestingly, the amount of storm-scale precipitation that falls subsequent to the recovery period is approximately proportional to the storm-scale intensity in the developing simulations. One possible reason for this is that Ekman pumping is stronger in the simulations with

stronger storm-scale circulations. Increased boundary layer forcing in these simulations could conceivably ignite more widespread convection than in the weaker simulations. Other possible reasons for the relationship between precipitation and system strength are shear-induced quasigeostrophic lift, which can depend on vortex strength (e.g., Frank and Ritchie 1999, 2001; Rogers et al. 2003; Jones 1995, 2000a,b), and differences in strength-dependent surface fluxes and cloud-base moisture. The full extent to which each of these contributes to precipitation rates is beyond the scope of this study.

5. Effects of moist convection: Local scales

Although the previous section showed that storm-scale quantities are well behaved in the sense that very small incremental changes in initial conditions produce incremental changes in storm-scale strength, local-scale strength metrics are less predictable. For example, maximum wind speed and vorticity vary strongly from one time to the next, and both variables tend to be higher in QRT3 than in QRT4 through QRT6, which are stronger on the system scale. Understanding local-scale behavior is particularly important for maximum wind speed because it is used operationally to classify tropical cyclones. This section explores precisely why local-scale metrics are less predictable and can give significantly different estimates of relative strength than their storm-scale counterparts might imply.

a. Divergence between QRT3 and QRT4

What physical processes lead to the seemingly chaotic result that QRT3 has the strongest peak winds (hurricane strength, greater than 32 m s^{-1} in Fig. 7d) despite having lower instability? First, recall from section 4 that the developing cyclone in QRT4 has *both* stronger updrafts and downdrafts during the first 6 h. Accompanying the strong downdrafts in QRT4 is low-θ_e air that quickly diminishes convective intensity near its center. We will show here that not only do the strong downdrafts in QRT4 diminish its convection, but they also catastrophically interfere with the collection of VHTs that builds the central core during the first 6 h. Thus, although the previous section shows that QRT4 has more storm-scale convection and is stronger on the storm scale, QRT3 has a better-organized core structure with strong, near-center VHTs and higher maximum winds for much of the period.

To answer the introductory question to this subsection, we first examine an early period before QRT3 and QRT4 strongly diverge, just after convection reaches its peak intensity (as determined by mean 700-hPa w in Fig. 7). Specifically, the first column of Fig. 11 shows the spatial distribution of updrafts and downdrafts in relation to the VHTs in both QRT3 and QRT4 at 5 h. Quite clearly, the initially stronger convection in QRT4 is associated with more numerous and stronger downdrafts in the vicinity of the central core than in QRT3. A band of downdraft wraps from southeast to north of the developing vorticity core in QRT4 (Fig. 11a), but in QRT3 the downdraft area is discontinuous and weaker (Fig. 11g). Associated with the encircling band of downdraft in QRT4 is a band of low-θ_e air at mid levels. The slightly lower θ_e near the center in QRT4 at 985 hPa (cf. Figs. 11d and 11j) is a sign that the effects of the downdraft have begun to reach the surface.

The formation of a convective line and an associated cold pool in QRT4 reduces QRT4 θ_e to even lower values. For instance, the middle column of Fig. 11 compares QRT3 and QRT4 at 7 h. After the downdraft on the north side of the core in QRT4 penetrates to the surface, a north–south-oriented convective line forms to the northwest of the center along the leading (western) boundary between high- and low-θ_e air (Fig. 11b,e). The convective line, which seems to form as a result of forcing along the θ_e boundary, lasts from about 6.5 to 8.5 h. Downdraft formation behind the line strongly reinforces the cold pool (Figs. 11e,f) and seems to be a primary reason why storm-scale surface θ_e decreases more in QRT4 than in QRT2 and QRT3 (which do not have such a line forced along the θ_e interface).

As a result of the widespread cold pool, the VHTs near the center of QRT4 lose their access to the most unstable air, their updrafts wane, and their vorticity cores begin to dissipate. The arrows in Figs. 11d–f point to the same 985-hPa vorticity anomaly from 5–9 h, which forms in the central VHT at 5 h. The anomaly and parent VHT at the center of Fig. 11d are quite strong at 5 h and are surrounded by multiple other VHTs within a few tens of kilometers. At 7 h, although there is another strong VHT just to its south, the VHT in Fig. 7e is nearly completely surrounding by low-θ_e air. Without access to unstable air, the updrafts and vorticity towers of both the original anomaly and the anomaly just to its south significantly weaken by 9 h. The cold pool in Fig. 11f spreads southward after 9 h, shoving convection and vorticity production even further from the center. Although updrafts occasionally fire over the QRT4 center between 9 and 13 h, they are short lived, and it remains unorganized until its boundary layer recovers sufficiently for sustained convection after 18 h (not shown).

The local-scale evolution in QRT3 is clearly much different than in QRT4, largely because QRT3 lacks the strong cold pool that forms in QRT4. With initially weaker updrafts from 4 to 5 h in QRT3 (Fig. 9), the compensating downdrafts and cold pool are weaker by
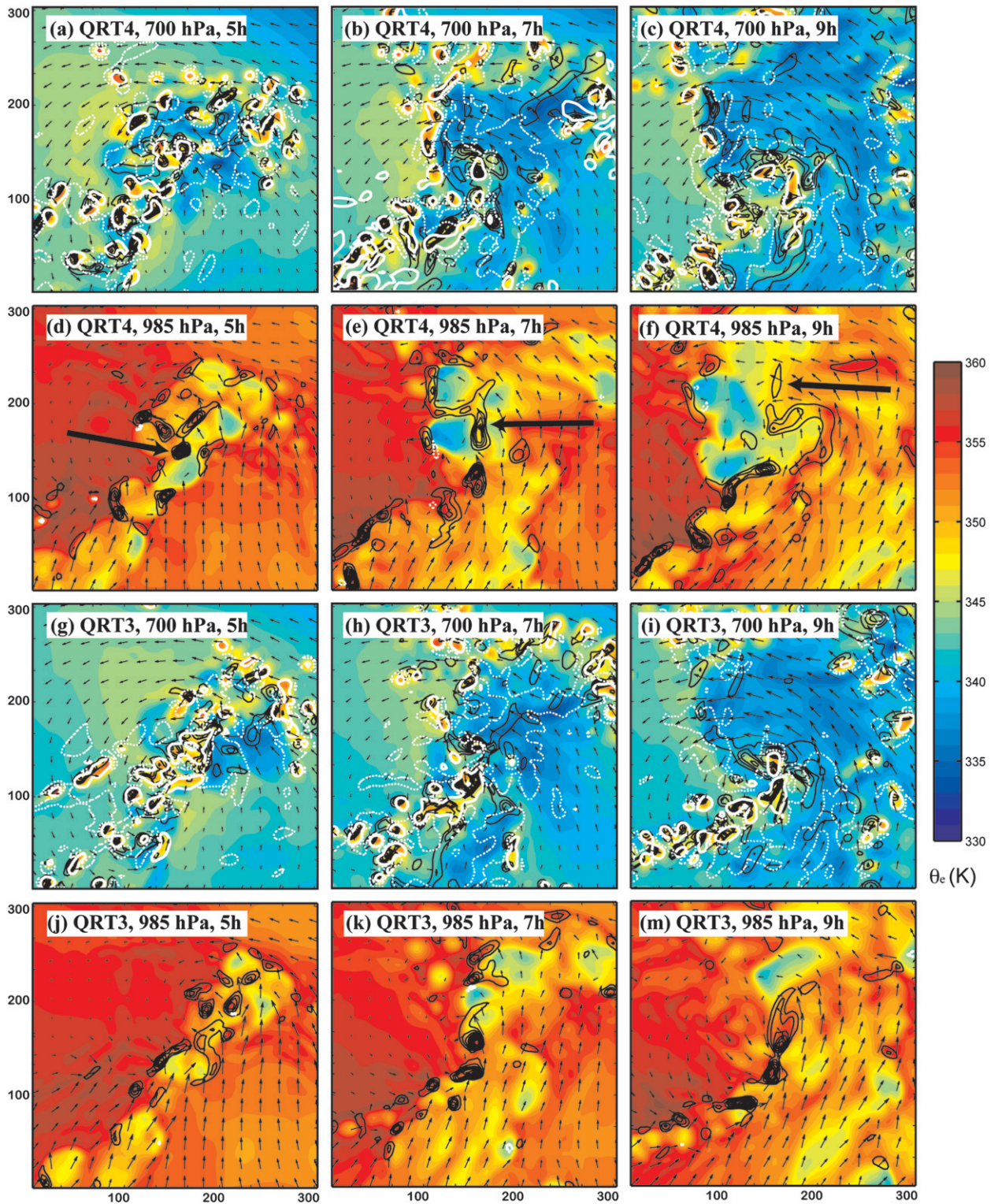
FIG. 11. As in Fig. 6, but all variables are displayed for the simulation, level, and time indicated in each panel. The arrows in (d)–(f) point to the same region of low-level vorticity originally associated with the strongest vorticity tower at 5 h.

5 h. Perhaps not coincidentally, a convective line fails to materialize along the edge of the weaker cold pool (Figs. 11h,k), although *some* convection does occur at that location. Without the convective line, significantly less low-θ_e air penetrates to the surface, and the conglomeration of VHTs near the center of QRT3 enjoys practically uninhibited access to the unstable air to its west and southwest. The effect on the QRT3 surface vorticity field is substantial in Figs. 11k–m, where a strong surface vorticity core builds beneath the 700-hPa anomaly. An additional factor that contributes to low-level vortex intensification in QRT3 is the merger of multiple VHTs. In QRT3 and QRT4, the western extension of an initial convergence line focuses further convection, and individual cells and associated vorticity anomalies in this region move northeastward toward the circulation center (see Fig. 11m). In QRT4 the spreading cold pool prevents these anomalies from reaching the center, but in QRT3 a number of these anomalies merge and strengthen the central vortex between 6 and 12 h. This multitude of factors leads to a sustained, organized core in QRT3 and helps QRT3 to ultimately develop the strongest maximum winds of all the simulations (Fig. 7d).

Despite the above differences, it should be remembered that QRT4 remains stronger than QRT3 in the storm-scale averages for the duration of the simulation because of its stronger storm-scale convection. Although downdraft activity significantly disrupts the core structure of QRT4, its high storm-scale vorticity provides an ideal environment for regeneration of an organized core after 24 h when convection reignites. By 36 h, the storm in QRT4 is well organized and rapidly approaching hurricane strength (see Figs. 5 and 7).

b. Divergence between QRT2 and QRT3

The previous subsection demonstrates that unobservable large-scale initial-condition differences between QRT3 and QRT4 result in strong differences in the intensity and placement of updrafts and cold pools. This eventually leads to a different route to tropical cyclogenesis between QRT3 and QRT4. The initial-condition difference between QRT2 and QRT3 is exactly the same as that between QRT3 and QRT4, and here we examine what physical processes lead to the failure of QRT2 in developing a well-organized tropical cyclone (e.g., Fig. 5b).

First, recall from Figs. 7 and 10 that storm-scale changes in strength correspond to incremental changes in initial conditions. Just as QRT4 has more initial storm-scale precipitation than QRT3 because of higher initial instability, QRT3 also has more precipitation than QRT2. Thus, while the inner core of QRT2 is

significantly less organized than QRT3 (Fig. 5), storm-scale differences between the two simulations are generally accounted for by the small difference in initial conditions.

In addition to being weaker on the storm scale, QRT2 is significantly weaker than QRT3 (and QRT4) on the local scale toward the end of the simulation (Fig. 7). The cause of the local-scale weakness appears to be the failure of QRT2 either to develop a strong background vorticity field or to maintain a well-organized vorticity core. Although the inability of QRT2 to maintain a strong core is initially similar to QRT4, an important difference between QRT2 and QRT4 is that QRT4 establishes a stronger storm-scale vortex during the first 6–12 h. Given exactly the same convection after the recovery period (i.e., after 24 h), QRT2 should take longer to re-establish a strong core than QRT4 because the storm-scale vorticity in QRT2 is considerably lower (and thus there is less potential for stretching deformation). Not only is the vorticity environment less favorable for strong VHT formation in QRT2, QRT2 also has less storm-scale convection/precipitation from 24 to 36 h (see section 4). Given that convection clearly contributes to VHT formation (e.g., Hendricks et al. 2004; Montgomery et al. 2006), it appears that a weaker vortex and less precipitation on the storm scale strongly limit the ability of QRT2 to develop a stronger core after 24 h. The remainder of this subsection will focus on the reasons why the original vorticity tower in QRT2 failed to maintain itself in the first place.

Surface cold pools ultimately lead to the destruction of the QRT2 original vorticity core (i.e., that which forms around 5 h and is clearly a strong vortex at the center in Figs. 12a,b and 13j), but the precise sequence of events here is somewhat different than in QRT4. Although low-θ_e air forms on the east side of the central VHT cluster in QRT2 as early as 7 h (Fig. 12b), this cold pool is to the east of VHTs, and the warm inflow from the southwest is not disrupted at this time. A few hours later, surface outflow from convection to the southwest of the QRT2 central VHTs is well positioned to disturb VHT inflow and suppress updrafts. After 9 h the convection in QRT2 shifts well to the southwest of the remnant vorticity center (Fig. 12c).

Upon the disruption of convection near the center in QRT2, vertical wind shear tears apart the low- to mid-level vortex. Figure 13, which shows data similar to Figs. 11 and 12 at 500 and 850 hPa, demonstrates the combined negative effects of surface cold pools and shear in QRT2. The surface cold pool disrupts the central conglomeration of VHTs, and the last updraft through the original low-level vorticity center diminishes around 9 h (Fig. 13j). Thereafter, the low-level core weakens (see
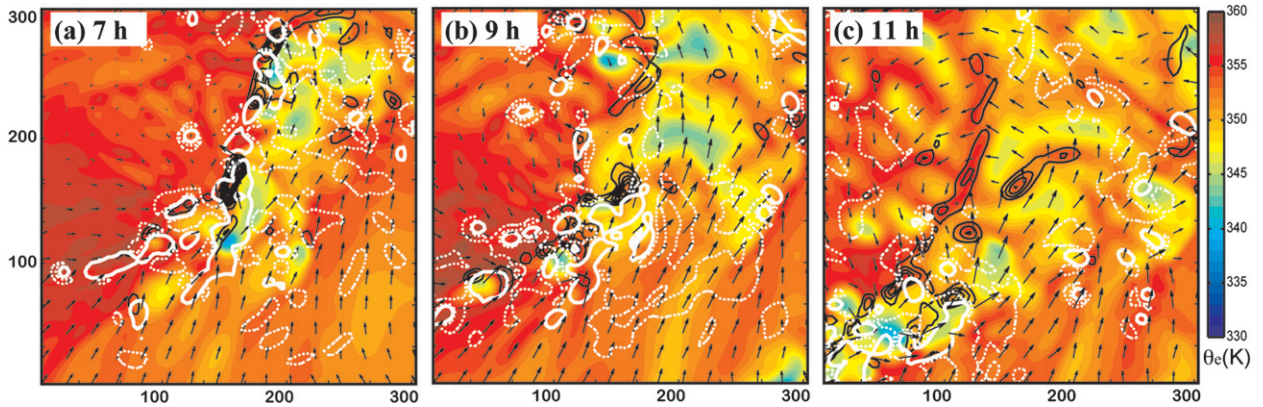
FIG. 12. As in Fig. 6, but variables are shown for QRT2 at the time indicated in each panel.

the arrows pointing to it in Figs. 11k–m), and the mid-level vortex advects to the southwest under the influence of northeasterly wind shear (Fig. 11h,i). Meanwhile, convective updrafts in QRT3 continue to strengthen its core well past 9 h (Figs. 13a–f), and its low-level vortex remains intact. A similar evolution to that seen in QRT2 and QRT3 (i.e., a "fight" between convection and wind shear for the strength of the vortex) was found in Tory et al. (2007).

In summary, this and the previous subsection demonstrate that unobservable large-scale initial-condition uncertainties may result in strong differences in the intensity and maintenance of VHTs and the core structure of tropical cyclones. In QRT2, the destruction of the initial vorticity core is particularly disastrous for the cyclone's later organization because the larger-scale vortex is weaker and less able to support the rapid redevelopment of another strong core. In some sense, these results demonstrate that QRT3 is an anomaly because surface cold pools lead to the demise of the core in QRT2 and QRT4, but not in QRT3. The cyclone in QRT3 seems to enjoy the benefits of more convection than QRT2, but it does not have quite enough convection (or quite the necessary convective mode) to develop the strong cold pool seen in QRT4. With a strong, low-level vortex intact through 24 h, the QRT3 cyclone is primed to establish a very strong central core by 36 h. Thus, small initial-condition differences can lead to different routes to tropical cyclogenesis (e.g., QRT3 and QRT4) or to differences in whether a strong central core ultimately forms (e.g., QRT2 and QRT3).

It is worth noting that there is also a similar progression from a weak to strong vortex obtained in the 30-km simulations. However, the strength of the tropical cyclone vortex in the 30-km QRT3 is more like the 3.3-km QRT2 than the 3.3-km QRT3 (Fig. 4). Nevertheless, there is a sharp transition from QRT2 (non-

developer) to QRT3 (developer) in the 30-km simulations, which also implies limited predictability. In the 30-km simulation, the sharp transition from QRT2 and QRT3 results more from the thresholds in moist instability and convective triggering. Although the localized convection triggered in the 30-km QRT3 is somewhat reminiscent of the VHT cluster in the 3.3-km run, the differences between QRT3 and QRT4 in 30KM are dissimilar from those in 3.3KM. The strong differences in downdraft intensity are absent in 30KM, so with slightly stronger convection, the QRT4 vortex is more intense even on the local scale. Yet, since the 3.3-km cloud-resolving simulations are likely to be more realistic, we have chosen not to include any detailed diagnostics from the 30-km simulations.

c. Simulations QRT5 and QRT6

Simulations QRT5 and QRT6 behave similarly to QRT4, although they do exhibit hints of QRT3 behavior. Like QRT4, they have strong, cold downdrafts near the initial conglomeration of VHTs, and they both develop a convective line with a substantial cold pool (which is still evident at 9 h in Figs. 6a,b). Also as in QRT4, the vorticity core that develops within the first 6 h of QRT5 and QRT6 is destroyed by the downdrafts.

The VHT-destroying downdrafts in QRT5 behave similarly to the downdrafts in QRT4, although the QRT5 downdrafts are colder. A similar convective line to that in QRT4 forms with very low-θ_e air behind it, and the initial vorticity core does not survive (the only trace of it in Fig. 6a is the decaying vorticity maximum 80 km northwest of A1). However, another VHT (B1 in Fig. 6a) advects into the storm-scale region around 6–7 h and is one of the stronger vortices present in QRT5. Updrafts more or less remain over B1 through 13 h, and the remnant vortex stays intact through 24 h and eventually becomes collocated with the storm-scale
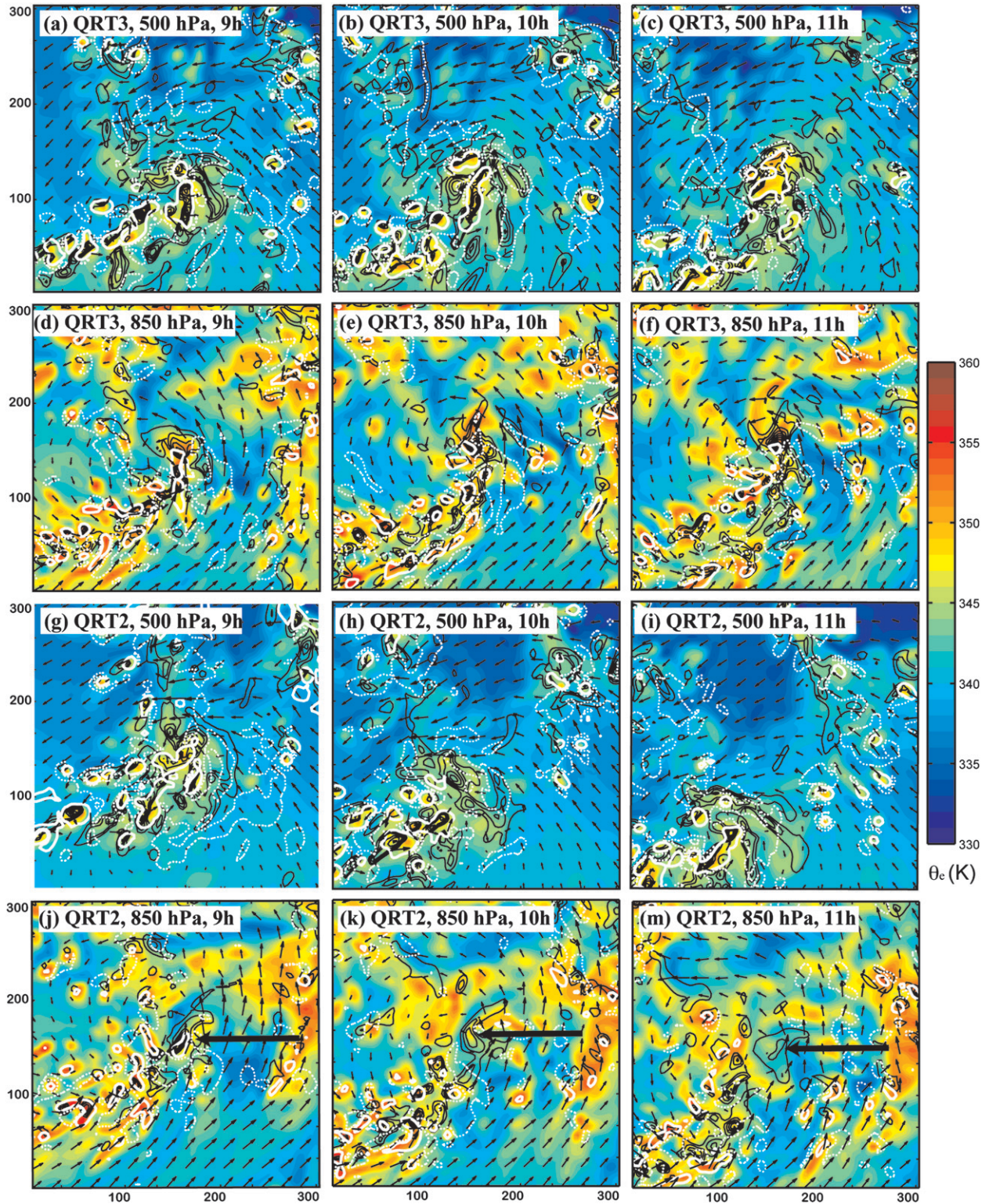
FIG. 13. As in Fig. 6, but all variables are displayed for the simulation, level, and time indicated at the top of each panel. The arrows in (j)–(m) point to the 850-hPa vortex associated with the strong central VHT cluster that forms around 5 h.

center. Around 20 h, new convection ignites over the remnant vortex, which is demarked by the arrow in Fig. 6c. At the same time that other strong vortices develop within nearby convection, the collection of vortices merge to form an even stronger center.

There are several differences between QRT5 and QRT6. First, initial downdrafts in QRT6 are even colder than those in QRT5. In fact, they are sufficient to extinguish the updraft of the primary vorticity before the convective line even forms (the vorticity remnants are no longer identifiable in Fig. 6b). Also, although VHT B2 advects into the storm-scale region of QRT6 similarly to B1 in QRT5, B2 never becomes associated with the storm-scale center. Rather, convection with B2 dissipates after 9 h, and its remnant vorticity decays. The low-level vorticity eventually associated with the system center in QRT6 can be traced back to a VHT that forms to the southwest of the initial QRT6 VHT as it decays around 6 h. Although its updrafts also diminish, its remnant low-level vorticity (A2 in Fig. 6b) becomes collocated with the storm-scale circulation center around 18–20 h, when a new round of updrafts results in a VHT cluster (Fig. 6d).

6. Summary and discussion

Through ensemble simulations and sensitivity experiments of a Gulf tropical disturbance, this study highlights the limited predictability that can be present in short-term tropical cyclone intensity forecasts given both realistic and minute analysis uncertainties in the large-scale environment. Strong sensitivity exists in simulations with a grid spacing of 30 km, which is comparable to that of global models used operationally for numerical guidance (using parameterized convection). Equally strong sensitivity is present with a cloud-resolving grid spacing of 3.3 km.

It is found that much of the extreme sensitivity herein is the result of how initial convection in the ensemble members responds to differences in the environment. The amount of convection early in the simulations, which is modulated by the initial convective instability, is instrumental in forming a deep vortex. Also, widespread cold convective downdrafts that form during the convection subsequently damp convective activity in a period that sees neither growth nor decay of the storm-scale vortices. After the boundary layer recovers, convection reignites and stronger storm-scale vortices strengthen more quickly.

Randomness in the details of small-scale convection may lead to differences in inner core organization and subsequent organization and growth to larger scales. Thus, the route to cyclogenesis can significantly depend

on the same small initial-condition differences. This result is due to chaotic interactions of convective and mesoscale features whose timing and placement significantly vary with slight initial differences. Initial differences can therefore more easily explain differences in simulated area-average quantities (such as average wind speed) than absolute quantities (such as maximum wind speed), implying that often-used absolute metrics of hurricane intensity have much more limited predictability.

The strong sensitivity exemplifies the inherent uncertainties in hurricane intensity prediction where moist convection is the key that limits predictability, a result similar to findings regarding extratropical winter snowstorms (Zhang et al. 2002, 2003, 2007) that complements the recent study on tropical cyclone predictability of Van Sang et al. (2008). Future studies should examine how additional initial uncertainties at smaller scales and errors in the forecast model, both of which are not considered in the current study, may further lead to even stronger forecast divergence. The current results are apparently limited by how accurately the 3.3-km simulations can faithfully represent the essential dynamics of moist convection. The impacts of model error can be partly seen in the apparent and significant difference between the 3.3- and 30-km simulations that use exactly the same initial conditions. These differences appear in spite of a similar trend in response to large-scale (sometimes immeasurable) differences in initial conditions (e.g., QRT2 and QRT3 in Fig. 4).

We must acknowledge that the limit of predictability of tropical cyclogenesis from this case study may not be true for all tropical cyclones. Future studies are also needed to examine the varying limits of tropical cyclone predictability under different flow regimes and stages of storm evolution. More work is also needed to determine the frequency of strong sensitivity to subtle changes in initial conditions seen here and to determine the impact of model spinup on the forecast sensitivity. Our preliminary analysis (not shown) suggests that several cases during the 2007 Atlantic hurricane season may have demonstrated similar sensitivity. These include, but are not limited to, Hurricanes Humberto and Lorenzo and Tropical Depression 13. These three cases coincidentally occurred near the Gulf Coast and presented extreme difficulty for operational forecasts of their formation and intensification.

The current study implies that the predictability of tropical cyclones may be strongly limited at all time scales, ranging from day 1 to long-term projections. This remains true regardless of whether one uses statistical methods or numerical weather and climate prediction models (e.g., Davis et al. 2008; Houze et al. 2007;

Oouchi et al. 2006). The limit of intensity predictability given realistic initial-condition and model errors (which are still large at present) in numerical weather prediction models may be alleviated through improving our understanding of dynamics and physics, development of better numerical models, and improved data coverage and assimilation techniques. However, there will always be forecast errors because of the inherent limit of predictability arising from initial errors with amplitudes far smaller than any observation and analysis system; these are errors with which society will always have to cope, more so given that coastal populations vulnerable to hurricanes are still on the rise (Pielke 1997).

Inherent uncertainties in hurricane forecasts illustrate the need for developing advanced ensemble prediction systems to provide event-dependent probabilistic forecasts and risk assessment. In practice, despite an increasing role and demonstrated benefits of using ensembles in aiding deterministic hurricane forecasting (Krishnamurti et al. 1999; Zhang et al. 2009), the uncertainty issued with today's operational hurricane forecasts is still based on averaged climatological errors and is not case dependent. Thus, this study also has strong implications related to how society might better distribute resources to combat future hurricane-related disasters given that the number of hurricanes and their intensity/destructiveness may be on the rise as a result of a warming climate (Emanuel 2005; Webster et al. 2005).

REFERENCES

Barker, D. M., 2005: Southern high-latitude ensemble data assimilation in the Antarctic mesoscale prediction system. *Mon. Wea. Rev.,* **133,** 3431–3449.

Bei, N., and F. Zhang, 2007: Mesoscale predictability of the torrential rainfall along the mei-yu front of China. *Quart. J. Roy. Meteor. Soc.,* **133,** 83–99.

Davis, C. A., and Coauthors, 2008: Prediction of landfalling hurricanes with the advanced hurricane WRF model. *Mon. Wea. Rev.,* **136,** 1990–2005.

Doswell, C. A., III, and E. N. Rasmussen, 1994: The effect of neglecting the virtual temperature correction on CAPE calculations. *Wea. Forecasting,* **9,** 625–629.

Dudhia, J., 1993: A nonhydrostatic version of the Penn State/NCAR mesoscale model: Validation tests and simulation of an Atlantic cyclone and cold front. *Mon. Wea. Rev.,* **121,** 1493–1513.

Elsberry, R. L., T. D. B. Lambert, and M. A. Boothe, 2007: Accuracy of Atlantic and eastern North Pacific tropical cyclone intensity forecast guidance. *Wea. Forecasting,* **22,** 747–762.

Emanuel, K. A., 1999: Thermodynamic control of hurricane intensity. *Nature,* **401,** 665–669.

——, 2005: Increasing destructiveness of tropical cyclones over the past 30 years. *Nature,* **436,** 686–688.

Frank, W. M., and E. A. Ritchie, 1999: Effects of environmental flow upon tropical cyclone structure. *Mon. Wea. Rev.,* **127,** 2044–2061.

——, and ——, 2001: Effects of vertical wind shear on the intensity and structure of numerically simulated hurricanes. *Mon. Wea. Rev.,* **129,** 2249–2269.

Franklin, J. L., 2004: National Hurricane Center verification report. *Proc. 57th Interdepartmental Hurricane Conf.,* Miami, FL, NOAA. [Available online at http://www.nhc.noaa.gov/verification/pdfs/Verification_2008.pdf.]

Hawblitzel, D., F. Zhang, Z. Meng, and C. A. Davis, 2007: Probabilistic evaluation of the dynamics and predictability of mesoscale convective vortex event of 10–13 June 2003. *Mon. Wea. Rev.,* **135,** 1544–1563.

Hendricks, E. A., M. T. Montgomery, and C. A. Davis, 2004: The role of "vortical" hot towers in the formation of Tropical Cyclone Diana (1984). *J. Atmos. Sci.,* **61,** 1209–1232.

Holland, G. J., 1997: The maximum potential intensity of tropical cyclones. *J. Atmos. Sci.,* **54,** 2519–2541.

Houze, R. A., S. S. Chen, B. F. Smull, W.-C. Lee, and M. M. Bell, 2007: Hurricane intensity and eyewall replacement. *Science,* **315,** 1235–1238.

Jones, S. C., 1995: The evolution of vortices in vertical shear: I: Initially barotropic vortices. *Quart. J. Roy. Meteor. Soc.,* **121,** 821–851.

——, 2000a: The evolution of vortices in vertical shear II: Large-scale asymmetries. *Quart. J. Roy. Meteor. Soc.,* **126,** 3137–3159.

——, 2000b: The evolution of vortices in vertical shear: III: Baroclinic vortices. *Quart. J. Roy. Meteor. Soc.,* **126,** 3161–3185.

Krishnamurti, T. N., C. M. Kishtawal, T. E. LaRow, D. R. Bachiochi, Z. Zhang, C. E. Williford, S. Gadgil, and S. Surendran, 1999: Improved weather and seasonal climate forecasts from multimodel superensemble. *Science,* **285,** 1548–1550.

——, S. Pattnaik, L. Stefanova, T. S. V. Kumar, B. P. Mackey, A. J. O'Shay, and R. J. Pasch, 2005: The hurricane intensity issue. *Mon. Wea. Rev.,* **133,** 1886–1912.

Montgomery, M. T., M. E. Nicholls, T. A. Cram, and A. B. Saunders, 2006: A vortical hot tower route to tropical cyclogenesis. *J. Atmos. Sci.,* **63,** 355–386.

Oouchi, K., H. Yoshimura, R. Mizuta, S. Kusunoki, and A. Noda, 2006: Tropical cyclone climatology in a global-warming climate as simulated in a 20-km mesh global atmospheric model: Frequency and wind intensity analyses. *J. Meteor. Soc. Japan,* **84,** 259–276.

Pielke, R. A., Jr., 1997: Reframing the U.S. hurricane problem. *Soc. Nat. Resour.,* **10,** 485–499.

——, J. Gratz, C. W. Landsea, D. Collins, M. Saunders, and R. Musulin, 2008: Normalized hurricane damages in the United States: 1900–2005. *Nat. Hazards Rev.,* **9,** 29–42.

Rogers, R., S. Chen, J. Tenerelli, and H. Willoughby, 2003: A numerical study of the impact of vertical shear on the distribution of rainfall in Hurricane Bonnie (1998). *Mon. Wea. Rev.,* **131,** 1577–1599.

Rotunno, R., and K. A. Emanuel, 1987: An air–sea interaction theory for tropical cyclones. Part II: Evolutionary study using a nonhydrostatic axisymmetric numerical model. *J. Atmos. Sci.,* **44,** 542–561.

Sippel, J. A., and F. Zhang, 2008: A probabilistic analysis of the dynamics and predictability of tropical cyclogenesis. *J. Atmos. Sci.,* **65,** 3440–3459.

——, J. W. Nielsen-Gammon, and S. E. Allen, 2006: The multiple-vortex nature of tropical cyclogenesis. *Mon. Wea. Rev.,* **134,** 1796–1814.

Tory, K. J., M. T. Montgomery, and N. E. Davidson, 2006a: Prediction and diagnosis of tropical cyclone formation in an NWP system. Part I: The critical role of vortex enhancement in deep convection. *J. Atmos. Sci.,* **63,** 3077–3090.

——, ——, ——, and J. D. Kepert, 2006b: Prediction and diagnosis of tropical cyclone formation in an NWP system. Part II: A diagnosis of Tropical Cyclone Chris formation. *J. Atmos. Sci.,* **63,** 3091–3113.

——, N. E. Davidson, and M. T. Montgomery, 2007: Prediction and diagnosis of tropical cyclone formation in an NWP system. Part III: Diagnosis of developing and nondeveloping storms. *J. Atmos. Sci.,* **64,** 3195–3213.

Van Sang, N., R. K. Smith, and M. T. Montgomery, 2008: Tropical-cyclone intensification and predictability in three dimensions. *Quart. J. Roy. Meteor. Soc.,* **134,** 563–582.

Webster, P. J., G. J. Holland, J. A. Curry, and H. -R. Chang, 2005: Changes in tropical cyclone number, duration, and intensity in a warming environment. *Science,* **309,** 1844–1846.

Willoughby, H. E., 1999: Hurricane heat engines. *Nature,* **401,** 649–650.

Zhang, F., C. Snyder, and R. Rotunno, 2002: Mesoscale predictability of the ''surprise'' snowstorm of 24–25 January 2000. *Mon. Wea. Rev.,* **130,** 1617–1632.

——, ——, and ——, 2003: Effects of moist convection on mesoscale predictability. *J. Atmos. Sci.,* **60,** 1173–1185.

——, A. Odins, and J. W. Nielsen-Gammon, 2006: Mesoscale predictability of an extreme warm-season rainfall event. *Wea. Forecasting,* **21,** 149–166.

——, N. Bei, R. Rotunno, C. Snyder, and C. C. Epifanio, 2007: Mesoscale predictability of moist baroclinic waves: Convection-permitting experiments and multistage error growth dynamics. *J. Atmos. Sci.,* **64,** 3579–3594.

——, Y. Weng, J. A. Sippel, Z. Meng, and C. H. Bishop, 2009: Cloud-resolving hurricane initialization and prediction through assimilation of Doppler radar observations with an ensemble Kalman filter: Humberto (2007). *Mon. Wea. Rev.,* in press.